Experimental observation of the collision of three vortex rings

2015 Fluid Dyn. Res. 47 035513

(http://iopscience.iop.org/1873-7005/47/3/035513)

IOP Publishing | The Japan Society of Fluid Mechanics Fluid *Dynamics* Research

Fluid Dyn. Res. **47** (2015) 035513 (21pp) doi:10.1088/0169-5983/47/3/035513

Experimental observation of the collision of three vortex rings

R H Hernández[1] and E Monsalve[2]

[1] LEAF-NL, Department of Mechanical Engineering, Universidad de Chile, Casilla 2777, Santiago, Chile
[2] ESPCI, 10 rue Vauquelin Paris 75005, France

E-mail: rohernan@ing.uchile.cl

Received 17 January 2015, revised 19 March 2015
Accepted for publication 28 March 2015
Published 15 May 2015

Communicated by William Roy Young

Abstract

We investigate for the first time the motion, interaction and simultaneous collision between three initially stable vortex rings arranged symmetrically, making an angle of 120 degrees between their straight path lines. We report results with laminar vortex rings in air and water obtained through measurements of the ring velocity field with a hot-wire anemometer, both in free flight and during the entire collision. In the air experiment, our flow visualizations allowed us to identify two main collision stages. A first ring-dominated stage where the rings slowdown progressively, increasing their diameter rapidly, followed by secondary vortex structures resulting after the rings make contact. Local portions of the vortex tubes of opposite circulation are coupled together thus creating local arm-like vortex structures moving radially in outward directions, rapidly dissipating kinetic energy. From a similar water experiment, we provide detailed shadowgraph visualizations of both the ring bubble and the full size collision, showing clearly the final expanding vortex structure. It is accurately resolved that the physical contact between vortex ring tubes gives rise to three symmetric expanding vortex arms but also the vortex reconnection of the top and lower vortex tubes. The central collision zone was found to have the lowest kinetic energy during the entire collision and therefore it can be identified as a safe zone. The preserved collision symmetries leading to the weak kinematic activity in the safe zone is the first step into the development of an intermittent hydrodynamic trap for small and lightweight particles.

Keywords: vortex rings, vortex dynamics, instabilities

(Some figures may appear in colour only in the online journal)

1. Introduction

The aim of this work was to produce symmetric collisions between three identical laminar and viscous vortex rings in order to create a localized and self-bounded spatial region to keep the flow vorticity and fluid fluctuations confined without the need of solid boundaries. A collision between two or more vortex structures is basically a time-dependent complex distribution of forces associated to individual momentum transfers (Cantwell 1986). The interest in colliding vortex structures can be traced back to the symmetric collisions between equal momentum vortex dipoles and the collision with solid walls (Heijst and Flor 1989, Voropayev and Afanasyev 1992).

To our knowledge, no previous investigation has determined the qualitative features of the flow structure when three rings collide simultaneously, however, the head-on collision and side-by-side collisions between two vortex rings have received great attention in the past (Fohl and Turner 1975, Oshima 1977). Here we were interested in the spatiotemporal flow structure produced by eventual merging of vortex tubes (Chatelain *et al* 2003) when the rings make contact at angles greater than the critical angle between typical side-by-side collisions (Fohl and Turner 1975). This kind of collision can restrain the ring interaction to a small spatial region due to the initial spatial symmetry, where the associated kinetic energy will be dissipated in short time scales, enhancing local mixing in a zone where the fluid was initially at rest.

This idea makes sense because vortex rings are self-propagating vortex structures, easy to create and very reproducible when working in the stable regime (Widnall and Sullivan 1973, Widnall and Tsai 1977). At low Reynolds numbers ($Re < 600$, based on ring velocity and ring diameter) vortex rings are laminar and stable, preserving their circular shape. Within these conditions, vortex rings can move in a straight path and it is possible to aim them into a specific target region in order to perform prescribed local measurements in that region. At a laboratory scale, it is pretty simple to create a ring by rapidly pushing a small amount of fluid through an orifice, and this simplicity with which to create these fascinating structures explains, in part, the large amount of research on vortex rings (see for instance the review of (Shariff and Leonard 1992)), however, symmetric collisions involving an odd number of rings are not reported in the literature.

Prior to any experiment with multiple rings one has to determine the individual behavior of single-vortex rings within a particular setup. Some ring properties, such as circulation or ring diameter versus time, may differ in situations where the rings move freely in unbounded (Hernández *et al* 2006) versus bounded (Stewart and Vlachos 2012) domains. Other internal conditions can also be also very relevant, such as the presence of non-zero radial velocity components during the initial ring formation, as this may produce dramatic changes in both ring circulation and final ring impulse (Krieg and Mohseni 2013). As rings carry momentum, their interaction with solid boundaries (Walker and Smith 1987) and with other classical fluid structures such as boundary layers have been reported in the literature (Arévalo *et al* 2010). In particular, the collision of vortex rings with a heated wall enhance the heat transfer, improving the efficiency of the system (Arévalo *et al* 2007). Another important concept is the role of rings in turbulence (Hwang and Eaton 2004). The interaction of vortex rings of multiple sizes, and the fact that they can easily reconnect when they collide, raises a question about the way the energy spectrum accounts for the variety of scale lengths produced by ring collisions of high kinetic energy (Chatelain *et al* 2003). The simplest version of ring collision is found in on-axis frontal collisions between two similar vortex rings where smaller rings are formed after reconnection, filling the energy spectrum with smaller scales (Lim and Nickels 1992). Ring collisions can be done in a very straightforward manner between two rings,

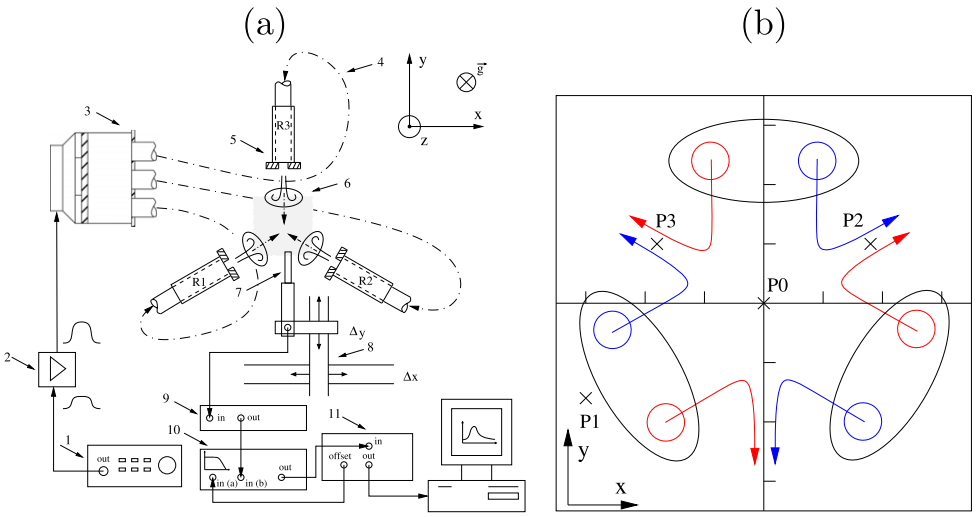

Figure 1. (a) The experimental set-up. A HP33120A function generator (1) provides the driving signal to a bipolar amplifier HSA4011 (2). The amplified signal pushes the piston in the pressure manifold (3) connected to 3 identical hydraulic hoses (4) that transmit a pressure pulse into each vortex generator of exit diameter $D_0 = 1.5$ cm (5). Vortex rings (6) of diameter D are created simultaneously, symmetrically and with great repeatability. Fluid velocity is measured with a hot-wire anemometer (7, 9) in a Cartesian spatial window of square grid size ($\pm 5D_0$, $\pm 5D_0$) controlled by a three-axis stepper motor system (0.48 mm/rev). (8) A preamplifier SR560 lowpass filters the signal which is acquired with a data acquisition card DT9804. (b) Ring collision diagram indicating spatial points where to compute statistics from time velocity series $P_0 = (0, 0, 0)$, $P_1 = (-30, -16.6, 0)$, $P_2 = (14, 8.75, 0)$, $P_3 = (-6, 7.9, 0)$ mm.

even with rings of different size, circulation and self-induced velocity (Arévalo 2010). However, to get smaller scales after a collision, one must increase the number of reconnections; one possibility would be to increase the ring's strength, however, this would probably trigger the ring's instabilities (Widnall and Tsai 1977).

An alternative is to make controlled collisions between many stable rings (i.e., with small Reynolds number) arranged into simple configurations in order to force specific vortex tube pairings and mergings during a collision (Arévalo 2010).

In the present work, we report different experiments in air and water, where three laminar and similar vortex rings collide simultaneously. They are launched by vortex generators located at the vertices of an imaginary equilateral triangle, aimed into the triangle center where a bounded collision occurs. We were motivated by the production of local velocity and vorticity fluctuations restricted to a self-bounded spatial region without the need of solid boundaries. This paper is organized as follows. Section 2 describes the experimental set-up and the properties of the rings produced in our experiment using air. Results for single-rings in air are presented in section 3.1. Results for the ring collision in air are presented in sections 3.2–3.4. The potential properties of a hydrodynamic trap are in section 3.5. Results from the water experiment are presented in section 3.6. Concluding remarks are summarized in section 4.

2. Experimental setup

Experiments were performed at the leaf-nl laboratory at the University of Chile. In figure 1 we display the complete experimental set-up in air. Three vortex rings of same diameter D and self-induced velocity U_0 are created in a still air chamber using three independent but identical vortex ring generators, with an exit orifice diameter $D_0 = 1.5$ cm. Three identical pipes (diameter 3.8 cm) connected to a cylindrical manifold transmit a pressure pulse which ultimately will drive each vortex generator. The ring generator manifold is a cylindrical cavity (internal diameter 22 cm) with a loudspeaker inside, where the membrane of the loudspeaker, coupled to a flat piston, pushes an air-slug volume through three pipes creating simultaneously a ring at the three exit orifices of the ring generators.

Some fractions of a second after the pressure pulse, a simultaneous pinch-off process occurs on the three vortex rings, which then move with the same speed toward a collision point P_0 (figure 1(b)), located symmetrically 10 diameters apart ($10D_0$) from each vortex generator. The relative intensity of the collision can be adjusted through the self-induced velocity of the rings, which can be set between 10 and 120 cm s^{-1} depending on the strength of the forcing signal (amplitude or rise time). Local velocity is measured with a calibrated TSI hot-wire probe (50 μm in diameter) operated with a constant temperature anemometer and located from the top with the wire in horizontal position. We are able to measure the absolute value of fluid velocity $|u(x, y, t)|$ over the horizontal x-y planes at different heights ($-6 < z/D_0 < 6$). Probe position (x, y, z) is carefully controlled by a 3-axis stepper motor system with resolution of 0.48 mm/rev in x, y, z coordinates. The hot-wire velocity signal (absolute value) is lowpass filtered (12 dB/Oct @ 1 kHz) and amplified with a Stanford Research SR 560 pre-amplifier and then sampled by a DT9804 Data Translation 250 kHz and 16 bits acquisition card. The filter cutoff frequency is high enough to record most of the fluid fluctuations during collision. The forcing signal is generated by a function generator (Hewlett Packard HP33120A), then amplified by a high-speed bipolar NF amplifier HSA 4011. An external trigger signal starts both the ring emission and the A/D sampling.

To make accurate point-measurements of the vortex ring velocity with a single probe, we (*i*) start a single 3-ring realization, (*ii*) perform the velocity measurement at an initial spatial position (x_i, y_j, z_k), (*iii*) wait a certain time (many seconds) until perturbations produced by the collision are completely wiped out, (*iv*) change probe position (in an x-y plane) without misalignment to start again. At this stage we have a single velocity signal in time, but this procedure can be repeated automatically to make an arbitrary number of $(n_x \times n_y)$ grid points of synchronous measurements in an x-y plane with a given spatial sub-millimetric resolution (typically $\Delta x = \Delta y = 0.48$ mm) producing finally a 4-D matrix of fluid velocity $|u(x, y, z, t)|$ (absolute values). The hot-wire probe is placed from above along the z-axis to reduce interference with the ring motion. The advantage of the stepper motor control system is to move the probe with an accuracy of a fraction of millimeter and to be able to make the return to the origin without any spatial lag. It is undoubtedly a slow but very accurate operation: a complete velocity field in an x-y plane enclosing the ring collision may take 24 h depending on the grid size. The stability of ring production was tested on the basis of successive measurements of flow velocity at different spatial locations, previously programmed on our stepper motor system. Velocity fluctuations of the order of 3% were found between measurements performed one day and repeated after one week.

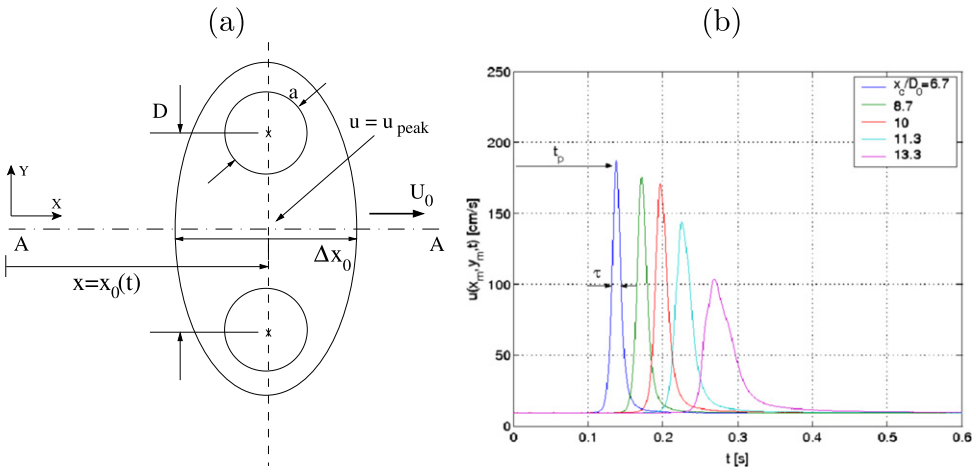

Figure 2. (a) Schematics of the position of a vortex ring. (b) Time series of velocity along the propagation direction, on centerline $A - A$ at different distances between the hot-wire probe and the vortex generator exit. Peak velocity occurs when the centroid x_0 of the ring moves across the hot-wire probe. The ring's flight time is indicated by the peak time t_p and the bubble width is related to the characteristic time τ.

3. Results

3.1. Single-ring properties in air

Before starting with ring collisions, we first characterized the ring generator measuring single-ring velocity profiles (from simultaneous measurements) with the hot-wire probe facing the ring as in figure 2(a). The idea is to record the two dimensional velocity profile map of a single-vortex ring in a y, z plane and verify typical ring properties near the ring generators within the collision setup. The rings exert a mutual influence when they are approaching the collision center which may cause both an increase in diameter and a decrease in their velocity. It is important to remark that synchronization is guaranteed because both data acquisition and ring emission (controlled pressure pulse) are triggered by a common external trigger signal and therefore the resultant 3D flow field can be consistently reproduced (Hernández *et al* 2006).

In order to determine the self-induced velocity of a ring, we must track its spatial position in time. A formal method to track the ring position in the reference system would be to compute (for instance) x_0, the centroid of z-vorticity, ω_z in an x, y plane as

$$x_0 = \frac{\int_S x\ \omega_z\ \mathrm{d}S}{\int_S \omega_z\ \mathrm{d}S} \tag{1}$$

calculated at each time step. But when the ring bubble is symmetric, this result is fairly similar to the position of the peak velocity in the propagation direction of the ring obtained from the time velocity series, making this method much more straightforward as it only requires the absolute value of fluid velocity. In figure 2 we show the concept describing the position of the ring through a continuous tracking of peak velocity across the ring's centerline. Peak velocity provides a precise estimation of the flight time spent by the ring when it moves between the

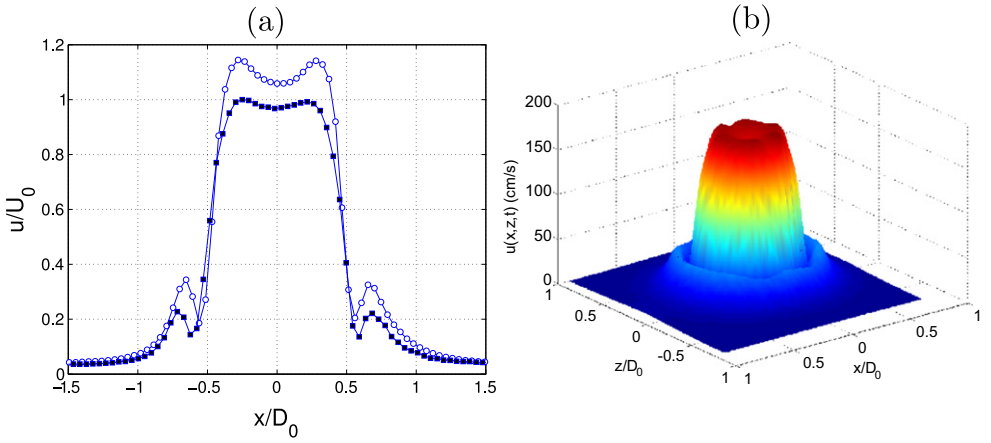

Figure 3. (a) Ring velocity profiles at $z = 0$ for two downstream locations, $L = D_0$ (∘) and $L = 4D_0$ (•). (b) 3D ring velocity map measured by a single local hot-wire probe, after 4900 realizations (70 × 70 grid points) of the same vortex ring which confirms both that our rings are stable and the procedure worked fine on the measurement plane as we get an axisymmetric velocity map.

exit orifice and the hot-wire probe. As a result we get a good estimation of the average self-induced velocity of the ring as

$$U_0 = x_0(t)/t_p \tag{2}$$

This ring velocity is not constant as shown in figure 2(b), and for $x_0/D_0 > 10$ the ring slows down and a velocity decrease of about 40% is observed. The distance travelled by each ring into the collision point is below $5D_0$; therefore the ring velocity inside the spatial window will be considered constant before collision effects take place. This procedure also provides a useful estimation of the averaged ring-bubble size, Δx_0, during the ring motion (figure 2(a) which is computed as $\langle \Delta x_0 \rangle = U_0\ \tau$ where τ is the characteristic time of each velocity signal in figure 2(b))

Local velocity measurements with a single hot-wire probe are shown in figure 3(a) for a single vortex ring at two downstream axial positions. A typical high velocity central bump is bounded by two sharp lateral minima (The hot-wire probe delivers the absolute value of flow velocity) followed by a decreasing irrotational region. The centers of rotation of the ring in such a plane correspond to those lateral minima, which are separated by almost a ring diameter. This is an interesting method as it provides a rough but quick estimate of the ring diameter during its motion and eventually during its interaction with other structures. An estimation of the vortex core size a to ring radius $R_0 = D_0/2$ with this method gives $a/R_0 \sim 0.5$ (see figure 3), a characteristic property of thick-cored rings (Sullivan *et al* 1973).

We want to recall the procedure described in detail in Arévalo *et al* (2007), and the necessary steps to get a complete velocity map with a single hot-wire probe: (i) after doing a single-ring realization, (ii) we perform the first point velocity measurement at (x_i, y_j, z_k), (iii) we wait 20 s to be sure that all fluid disturbances are damped out, (iv) then we change the probe position (x, y, z) to send a new identical ring. At this point we have a single velocity signal in time in one spatial location. This can be repeated automatically to make a scanning of an x-y spatial window performing synchronous measurements in constant spatial steps. The velocity map of figure 3(b) was obtained with this method, scanning a spatial window of

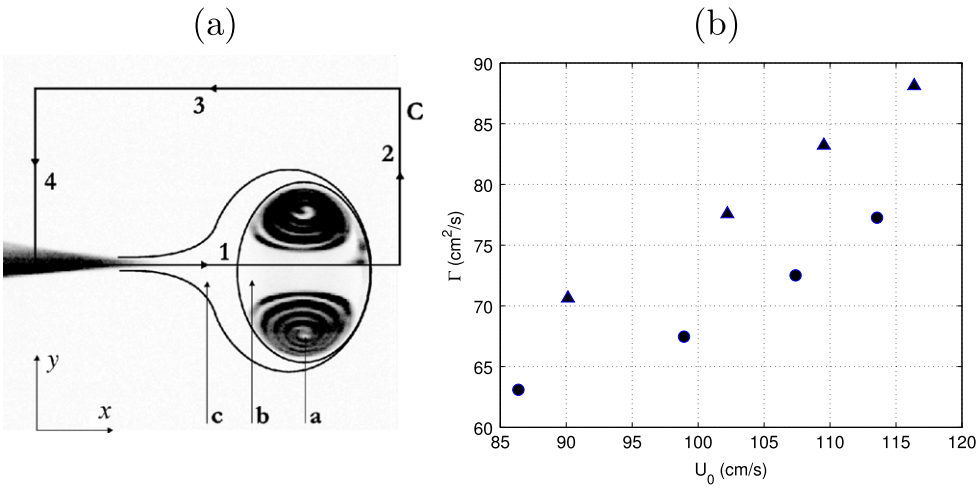

Figure 4. (a) A sketch of the contour path C to evaluate the ring's circulation Γ superimposed onto a ring image showing the bubble, vortex core and wake. (b) Ring circulation as a function of self-induced velocity measured on single-rings at $x/D_0 = 6.7$ (▲) and $x/D_0 = 10$ (•).

$2D_0 \times 2D_0$ corresponding to 70×70 grid points after 4900 realizations of the same vortex ring (spatial steps $\Delta x = \Delta y = 0.48$ mm). Similar hot-wire velocity measurements can be found in the literature to characterize the time evolution of basic properties of similar vortex rings in free motion (Hernández *et al* 2006).

Within the important properties of the *a* ring we have circulation or strength defined as,

$$\Gamma = \oint_C \mathbf{u} \cdot \mathrm{d}\mathbf{l} \tag{3}$$

which can be computed as in (Sullivan *et al* 1973), using the local velocity in the frame moving with the vortex ring, i.e., $u(x, y, t) \rightarrow u(x, y, t) - U_0$. Note that the self-induced velocity U_0 must be previously determined as described in figure 2 using equation (2). In the path C sketched in figure 4(a), the ring's circulation is calculated as an approximation of equation (3) at fixed z,

$$\Gamma(t) \sim \int_1 u_x(x, y, t)\, \mathrm{d}x \tag{4}$$

because the fluid velocity vanishes far from the ring. To do this, we need to transform the temporal signal $u(t)$ into a spatial signal $u(x)$, changing the time axis by a spatial axis using the self-induced velocity U_0. As shown in figure 4(b), Γ increases linearly with the self-induced velocity, keeping the same slope at two different downstream locations as expected. This approximation is accurate when the velocity is measured precisely on the spatial symmetry axis of a ring, such that we get only one component of velocity in the direction of ring motion.

3.2. Ring collision in air

In the present section we investigate symmetric collisions of three vortex rings in air under the schematic arrangement described in figure 1. Each collision can be characterized by the Reynolds number of a ring defined in terms of self-induced velocity as $Re = U_0 D_0/\nu$, where ν

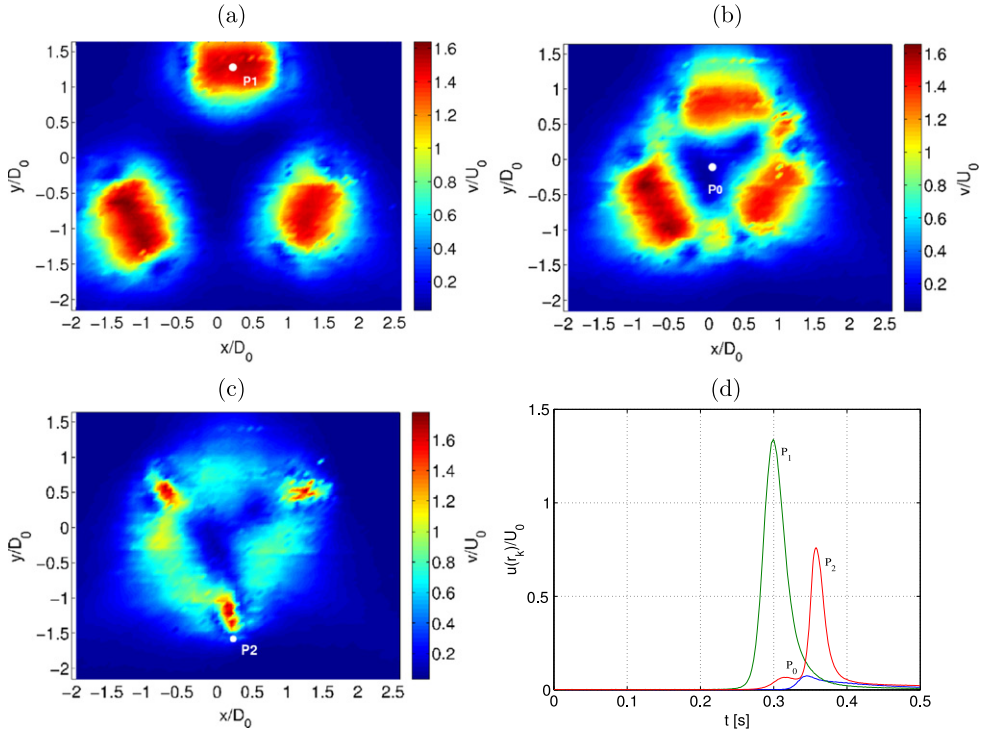

Figure 5. (a) Contour plot of velocity in an x, y plane at $t = 0.30$ s. We observe the position, size, and velocity level of each ring in that time instant. $Re = 500$, $D_0 = 1.5$ cm and $U_0 = 50$ cm s^{-1}. (b) $t = 0.32$ s. (c) $t = 0.34$ s. (d) Velocity time series at given spatial points (white dots) on each figure: collision center (P_0), center of the incoming top ring (P_1) and for the outward flow (P_2).

is the kinematic viscosity of the fluid in standard conditions. We are going to understand some fluid dynamical properties of the collision with the aid of both flow visualizations and local measurements of fluid velocity, based on the same single-probe procedure described in the previous section.

When the forcing signal drives the piston inside the pressure manifold, the relatively small stroke of the piston, combined with an important surface, is enough to create vortex rings simultaneously at the exit orifice on each vortex generator. We consider the rising edge of a TTL trigger signal as the time origin for the vortex ring formation. Repeatability is the key of our method, i.e. after each piston stroke we must have almost the same ring properties; otherwise the coherence between measurements could be lost. At low Reynolds numbers, $Re \sim 500$, we obtain stable rings which propagate while preserving their circular shape, and differences in normalized rms velocity fluctuations between different measurements carried out with one day of delay fall below 3% (under the same conditions). We know that repeatability and simultaneity of ring formation are by far the most important conditions that should be fulfilled in order to study the collision seriously. As shown in the schematic view of figure 1, what we expect at low Re is to have colliding rings that could preserve the 120° symmetry before the overall motion vanishes.

At low Re, in order to capture the complete collision, the best results are obtained with time series of 2 s of duration, including the overall motion of the ring, collision, reconnection,

and overall energy dissipation. In the *x*-*y* plane shown in figure 5, the hot-wire probe moves over a square measurement region of size $5D_0 \times 5D_0$ around the collision point P_0. A complete scan of the collision zone is equivalent here to cover 70 × 70 independent grid points where we store local fluid velocity. That means we must perform 4900 realizations of the collision stored into the 4-D matrix from which we can extract the free motion and mutual interaction of the rings in a given plane and at a given time. In figure 5 the contour plot of velocity corresponds to an *x*-*y* plane at mid-height $z = 0$ showing the time sequence of the collision at time intervals of $\Delta t = 0.02$ s. We see each vortex ring here represented by an intense spot where peak velocity is found near the spot's center.

Inside the spatial window, the progressive mutual influence between rings produces a reversed fluid flow. At first, vortex rings are seen as high velocity bumps which are moving inward, into the collision point P_0 in figures 5(a) and (b). But in figure 5(c), the vortex tubes of each ring make contact, where the local vorticity vectors have the opposite sign (Afanasyev and Korabel 2004), generating three new regions of outward flow velocity, keeping overall symmetry in the *x*-*y* plane making also a relative angle of 120°, but rotated 60° with respect to the original path. The mutual influence between rings can be evaluated quantitatively when we extract the respective time series from the 4D velocity matrix at any desired time. To know exactly where a ring is, we can find the the peak velocity and associated time instant in every spatial grid point. In figure 5(d) we display the time series of velocity in three grid locations, P_0, P_1, P_2, indicated by a white dot on each sub-figure. Each curve corresponds to the local velocity at a given grid location and is characteristic of a collision stage. The inward peak flow velocity at P_1 occurs first, followed by the lowest velocity at the collision central point at P_0, and finally the peak flow velocity at point P_2, where paired vortex tubes of opposite circulation turn into an arm-like vortex structure, responsible for the radially expanding motion. During the collision an important portion of the center zone surrounding the collision point (figure 5(b)) remains undisturbed (almost at rest), displaying a very weak kinematic activity, even though it is surrounded by strong fluid disturbances during the entire collision.

3.3. Secondary flow structures in air

The secondary flow structures formed during collision were also characterized with the aid of flow visualizations and local measurements of their velocity profiles at particular spatial locations. In figure 6 we show a flow visualization of the collision using smoke as a tracer and laser light sheets to illuminate a horizontal plane at $z = 0$. Vortex ring cores are seen here as black spots of high smoke concentration. Four successive time instants of the collision show the progression of each ring in the x, y plane. When the rings are very close we note that the vorticity of two side-by-side rings has an opposite sign leading to a local coupling between adjacent ring portions. After that, the outward flow ejections produced are responsible of the overall radial expansion of the flow at bisecting relative angles (cf figures 6(c) and (d)).

The flow structure associated with each of the flow ejections is in fact a vortex structure whose outward motion starts after the pairing of ring's vortex tubes with the opposite circulation strength ($\pm\Gamma$). Note that, as the incoming rings expand in diameter in their course to point P_0, the portions of each ring making contact with both neighbors increases as they become close to each other. In figure 7 we display a close-up of iso-velocity contour plots during the formation of the expanding structure at successive time instants crossing the coordinate axis $\sigma(x, y)$. During the ring approach into collision center P_0 we identify the pairing of the side-by-side vortex tubes as the mechanism responsible for the creation of this secondary structure.

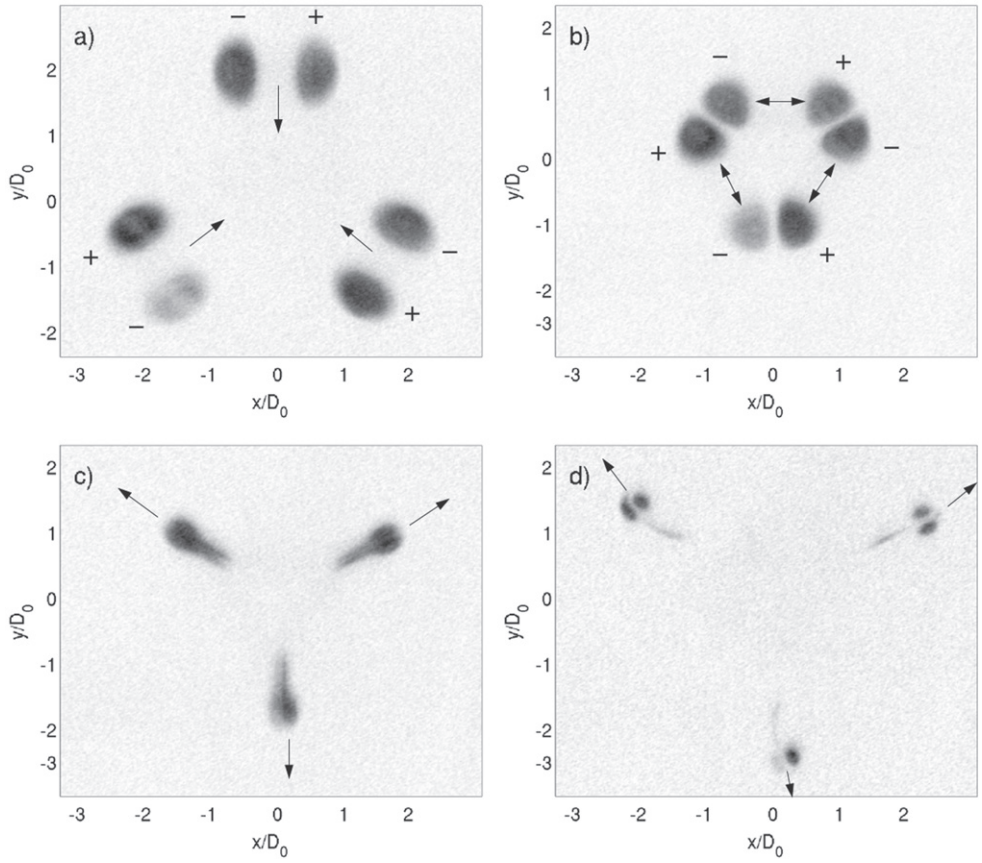

Figure 6. Flow visualization of the collision at mid-vertical plane ($z/D_0 = 0$) using a laser light sheet and smoke particles as a tracer. Smoke is concentrated inside each vortex bubble, which is marked with opposite signs of local vorticity. The expanding arms formed by vortex pairing, are indicated with arrows. (a) $t = 0.25$ s, (b) $t = 0.32$ s, (c) $t = 0.35$ s and (d) $t = 0.42$ s. $Re = 650$, $D_0 = 1.5$ cm.

The local velocity profiles (absolute values) of the secondary vortex structure are shown in figure 7(b). From the initial to the last stages, the velocity profile becomes progressively narrower, evolving into the shape similar to a vortex pair structure (see for instance Leweke and Williamson (1998)). The relative peak velocity is high compared to the initial self-advection velocity of the rings which explains the rapid expansion of the resulting arm-like vortex structures. The final structure width observed over each arm is roughly half of the initial ring diameter D_0, i.e. rather thick structures.

Flow visualization of secondary vortex rings is possible by switching the laser light plane into a new vertical position or height z, aiming into different zones of the collision sequence. In figure 8 the first part of the top (and bottom) reconnection pattern after collision is an initially triangular vortex structure evolving into an upward (downward) new vortex ring. At height $z/D_0 = 5.6$ cm (cf figure 8(d)), on top of the collision zone, we identify a vortex ring moving upward in the z-direction (figures 7(c) and (d)). As the collision and the reconnection process are both symmetrical with respect to the $z = 0$ plane, there is a similar ring moving

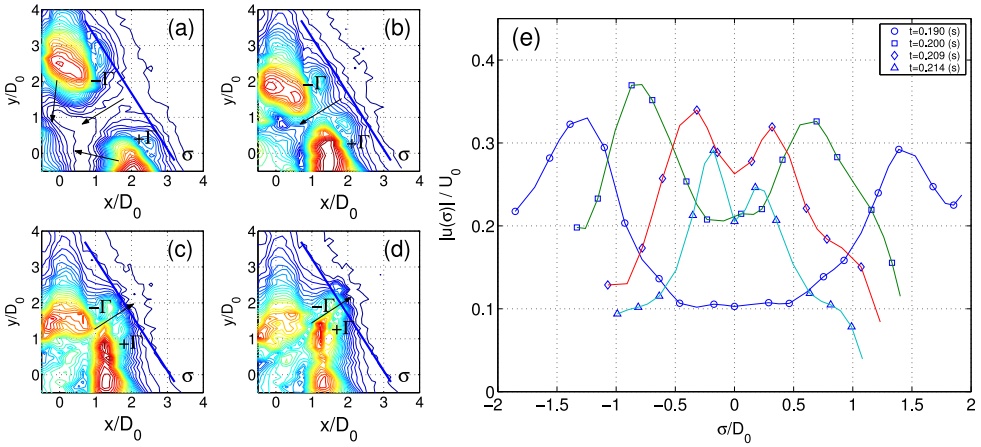

Figure 7. Vortex structure during lateral pairing of side-by-side ring vortex tubes. Contour plots of absolute values of flow velocity at the mid plane near point P_2 at $Re \sim 500$ for (a) $t = 0.190$ s, (b) $t = 0.200$ s, (c) $t = 0.209$ s, (d) $t = 0.214$ s. (e) Time sequence of lateral pairing of ring vortex tubes. We plot velocity profiles of a forming vortex structure at successive time instants. We plot absolute values of flow velocity ($|u(\sigma)|$) across the $\sigma(x, y)$ axis at the mid plane $z = 0$ near point P_2.

downward in the lower side of the collision ($z < 0$). In order to determine the size and velocity of these structures we performed local measurements at different heights z.

Velocity profiles of the secondary ring structures of figure 8 are shown in figure 9, where we show the contour plots of velocity at different time instants in the formation of the top secondary ring structure which moves in the upward direction. The velocity map at $z/D_0 = 1$ confirms the reconnection of the top sections of the vortex tubes of the three rings, giving rise to a high-velocity triangular vorticity structure advancing very rapidly in the z-direction. The triangular shape is observed at $z/D_0 = 1$ and $z/D_0 = 2$, and finally evolves into a big circular vortex ring (size $\sim 2D_0$) measured at $z/D_0 = 3$. We observe a similarity with the velocity profiles of individual initial rings of figure 3, especially where local sharp lateral minima are present, even at $z/D_0 = 1$ when the structure is still triangular. The velocity profiles of figure 9 indicate a consistent velocity reduction of the evolving upward ring as a result of its increased size.

After combining all the previous results, we offer a schematic explanation of the evolution of the collision in figure 10. The three rings approach the collision zone under a mutual ring influence, which is noted by the ring deceleration and consequent growth in diameter.

Once they make contact, lateral portions of side-by-side rings create vortex expanding structures in the form of arched arms that facilitate the successive expansion of the whole vortex structure. The reconnection of top and bottom portions of the three rings make a nearly triangular vortex tube appear, which rapidly evolves into a vortex ring moving upward for $z > 0$ (and downwards for $z < 0$ respectively). This schematic representation of the collision only helps us to describe the different collision stages. A more rigorous attempt to describe the kinematics of the post-collision vortex structures would require a mathematical formalism similar to the work of (Voropayev *et al* 2003), which would be valid for low Reynolds numbers.

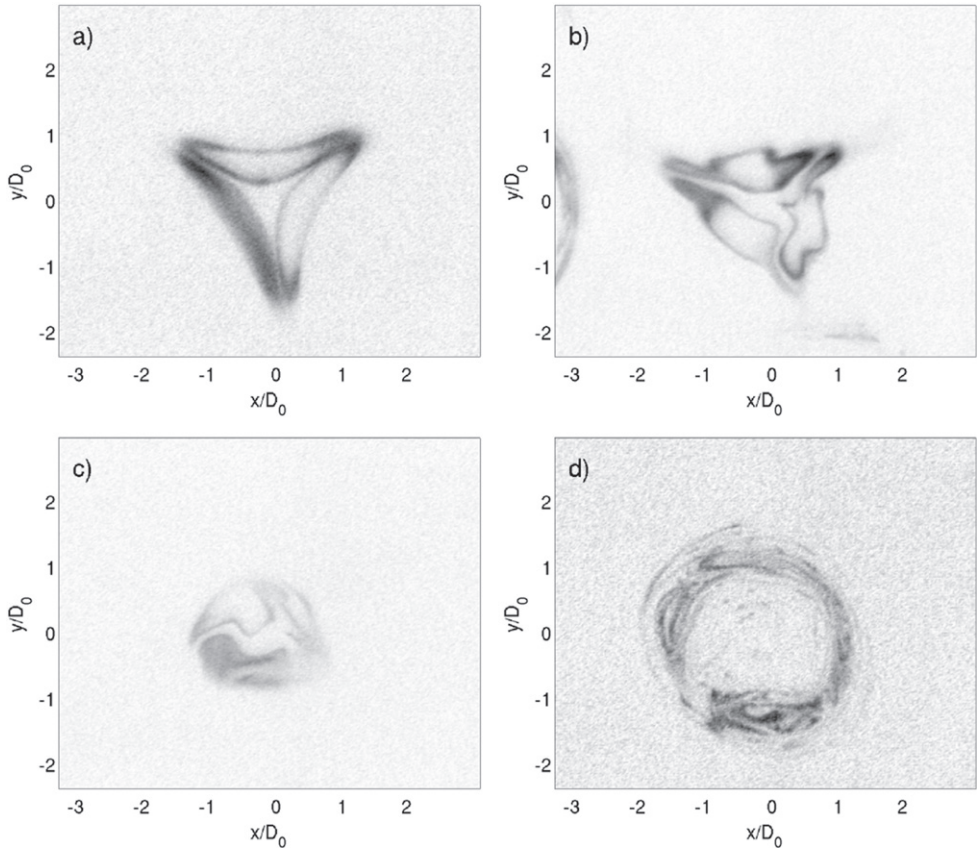

Figure 8. Images of the reconnection of vortex tubes at x, y planes with different heights ($Re = 650$). (a) $z/D_0 = 0.9$, $t = 0.350$ s. (b) $z/D_0 = 1.6$, $t = 0.415$ s. (c) $z/D_0 = 2.3$, $t = 0.415$ s (d) $z/D_0 = 5.6$, $t = 1.370$ s. We see here a new vortex ring moving upward.

3.4. Energy and power spectral density

The mutual ring influence produces a significant slowing down and diameter increase on every ring well before they make contact, which is followed by the vortex tube reconnection. In figure 11(a) we show five (enumerated) time series of velocity of an incoming ring taken at five equidistant spatial points between P_1 and P_0 along its trajectory into the collision point P_0. The velocity signal changes rapidly, both in peak amplitude and width as the ring slows down due to the presence of other two. However, the ring's bubble size, which can be determined from the characteristic time τ (full width at half maximum) of the time series, was found very close to D_0 and remains constant. In this process the kinetic energy of each primary vortex ring is dissipated during the collision, where the total kinetic energy displays a monotonic decrease in time. The total kinetic energy (per unit length) in a horizontal x-y single plane at fixed z, can be written as

$$E_k(t) = \frac{1}{2}\rho \int\int |u(t, x, y)|^2 \mathrm{d}x\mathrm{d}y \tag{5}$$

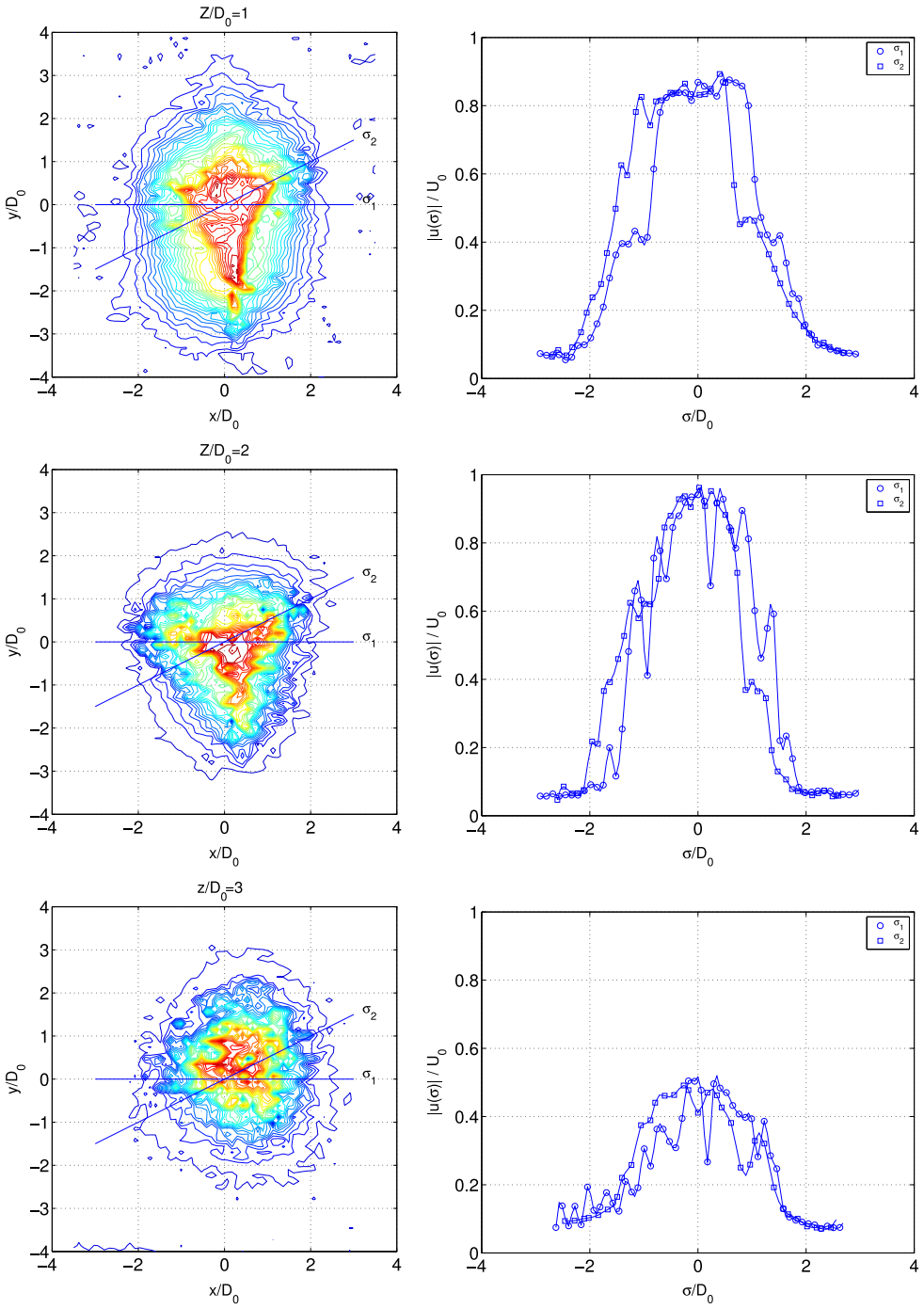

Figure 9. Evolution of the secondary vortex rings with height z and time at $Re = 320$. We plot contours of velocity (left) showing a first triangular shape vortex structure at $z/D_0 = 1$, 2 evolving into a circular vortex ring at $z/D_0 = 3$. We plot velocity profiles (right) of absolute values of flow velocity ($|u(\sigma)|$) across the $\sigma(x, y)$ axes defined on each contour plot.

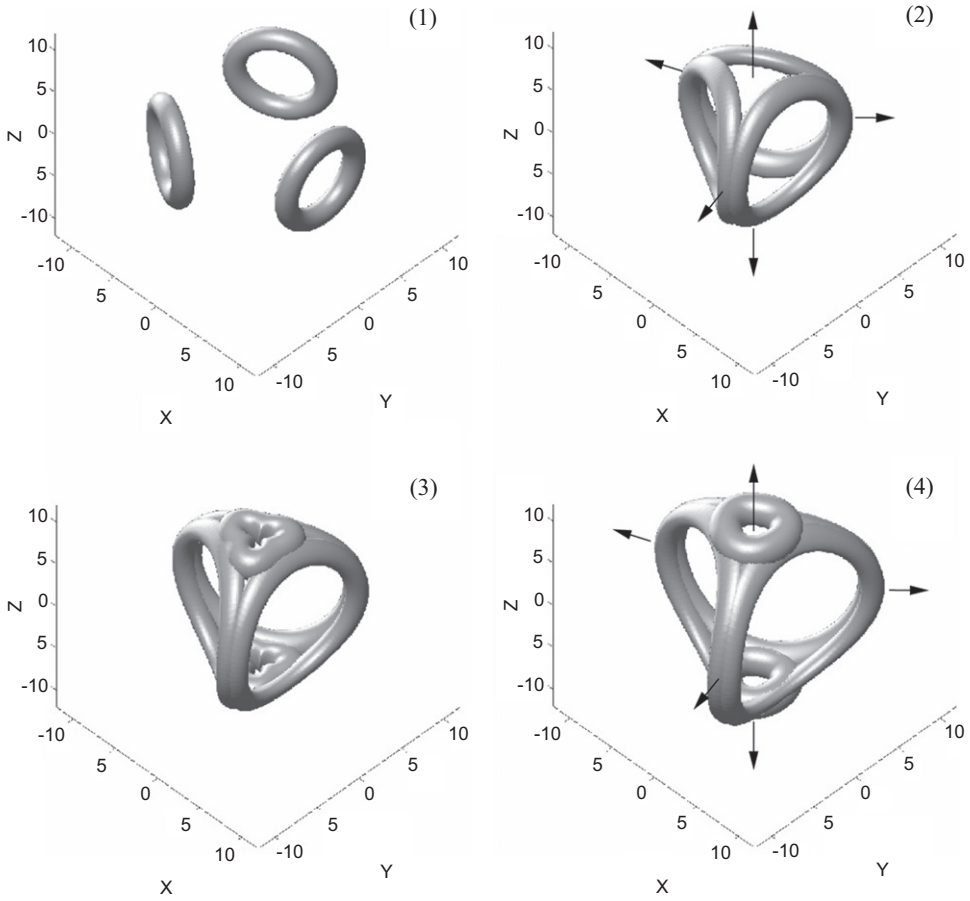

Figure 10. Schematic representation of the collision and reconnection of vortex tubes at successive time instants. (1) Laminar rings approaching collision point P_0. (2) Rings make contact, mutual ring influence and pairing starts. (3) Growth and reverse motion (expansion) of the structure and formation of secondary structures. (4) Two small rings moving upward and downward as well as the formation of arched expanding vortex structures.

We can compute $E_k(t)$ on the spatial window capturing the entire collision at successive time instants. This quantity is shown in figure 11(b) at four values of the Reynolds number, always keeping laminar and stable rings before they collide. Although the collision dissipates the kinetic energy very rapidly, it displays a marked dependence on the Reynolds number at first, during the ring-dominated stage. Then it follows a similar evolution during the next stage dominated by the secondary structures, as all curves start to collapse (after a given time) with little regard for the initial amplitude. To evaluate this we estimate the time derivative of the equation (5) which in fact represents the energy dissipation rate of an incompressible fluid in an unbounded domain. The slope at the inflection point of the curve provides a rough estimate of the dissipation rate as $\mathrm{d}E_k/\mathrm{d}t$ for each collision. As we can see in the inset of figure 11(b), the slope of each curve becomes steeper as the Reynolds number increases.

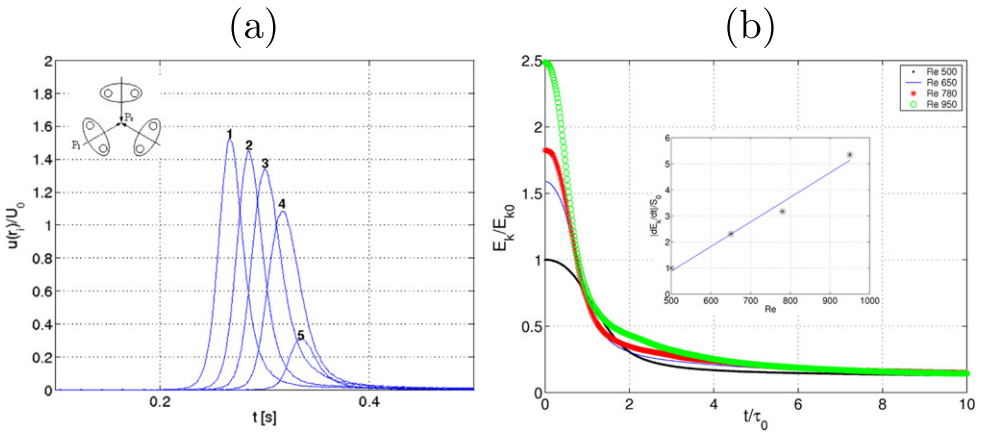

Figure 11. (a) Velocity of an incoming ring along its trajectory into the collision, taken at five (equidistant and numbered) spatial points between P_1 and P_0. The lower amplitude time series was taken at the collision center (P_0). (b) Spatially averaged kinetic energy $E_k(t)$ on the experimental window versus time for different Reynolds numbers. E_{k0} is the initial energy at the lowest Reynolds number (i.e., $E_k(t=0)$ at $Re = 500$) and τ_0 is time at the inflection point. In the inset we show the normalized energy dissipation rate $|\mathrm{d}(E_k)/\mathrm{d}t|/S_0$ of each curve versus Reynolds and a best fit. The reference slope of $E_k(\tau_0)$ at $Re = 500$ is S_0.

Higher initial ring velocities imply the collision starts at shorter times, marking a change in the way the kinetic energy is dissipated before and after the inflection point of each curve.

The kind of vortex structures dominating pre- and post-collision stages are responsible for the change in the energy curves of figure 11. But the way the energy is distributed across both spatial and time scales becomes clear when we look at the power spectral density of the local time velocity series. After a collision–reconnection event, the power spectral density should display some traces of the creation of new (smaller) vortex structures (Chatelain *et al* 2003). From the time series of velocity we compute the power spectral density at different instants of the collision, at different spatial locations of the collision region (cf figure 1).

The power spectral density of velocity is $P_u(f) = |\hat{u}(f)|^2$ where $\hat{u}(f)$ is the Fourier transform given by

$$\hat{u}(f) = \int_{-\infty}^{+\infty} e^{-2\pi i f t}\, u(t)\, \mathrm{d}t \tag{6}$$

In figure 12(a) we display the normalized power spectral density of absolute velocity at point P_1 which lies in the trajectory of one of the rings. We did four complete collisions at each Reynolds number, and at low frequencies the energy content does not reveal important differences. However, the energy clearly increases with Reynolds number below 100 (Hz), as the collision frequency bandwidth is relatively narrow. In figure 12(b) the power spectral density at the collision point P_0 indicates lowest energy levels, which are related to the very small flow fluctuations after collision compared to peak flow velocity. This could be understood by the fact that P_0 behaves as a stagnation point of the system as a result of the flow symmetry during the experiment.

Inside the collision frequency bandwidth, $10 < f < 100$ (Hz), energy is distributed toward higher frequencies when *Re* increases. This evident energy increase is associated with

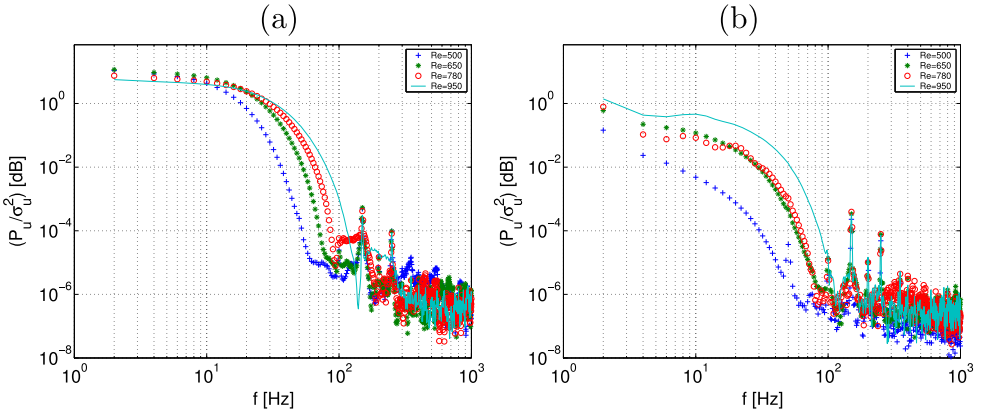

Figure 12. Normalized power spectral density of time series of velocity $P_u(f)/\sigma_u^2$ at specific spatial points. (a) $P_1 = (30, -16.6, 0)$ mm and (b) $P_0 = (0, 0, 0)$ mm. Here σ_u^2 is the variance of the time series of velocity at center collision point P_0 and lowest Reynolds number.

the creation of new, rapid and small-scale vortex structures feeding energy into moderate higher frequencies but, as restrictions due to the flow symmetries found, kept the overall flow with zero mean velocity (Hwang and Eaton 2004). The frequency peaks appearing in both figures at $f > 100$ (Hz) are harmonics originated by the electrical power source of the anemometer.

3.5. Potential use: Hydrodynamic trap

A flow structure with zero mean velocity can be regarded as a trap. An interesting key feature of the collision is to consider the center region (safe zone) as a tridimensional hydrodynamic trap, where the local shear or inertial forces make it possible to keep a small particle (fluid drops, flocs or solid particles) trapped in a stationary position (Tanyeri *et al* 2010). The idea of the hydrodynamic trap is not new; it can be traced back to the four-roll mill invented by Taylor (Taylor 1934), a device capable of generating a variety of flows from purely extensional to purely rotational through the appropriate motion of four cylindrical rollers. Further versions of the device using modern feedback control (Bentley and Leal 1986) made it possible to create shear flows able to capture particles in the vicinity of the stagnation point for long periods. In our case, the symmetry of the ring collision defines a center stagnation point and a safe zone *without the need of moving solid boundaries*. We have identified a safe zone around the collision point of very low kinetic activity with an estimated size $r_0 \sim D_0/5$. The region size does not change appreciably in the range of Reynolds numbers investigated here, however it clearly depends on the vortex ring diameter.

The kinetic energy in a disk of radius r, at a given instant t, can be written as

$$E_k(r, t) = \frac{1}{2}\rho \int_0^{2\pi} \int_0^r |u(r, t)|^2 \, r\mathrm{d}r\mathrm{d}\theta$$

From this definition we compute the time-averaged safe zone energy on a disk of fixed radius r_0 centered on the collision point as $E_k(r_0) = \langle E_k(r, t)\rangle$, where the brackets $\langle\ \rangle$ indicate time average and the upper limit r_0 is found as the cutoff below which the kinetic energy of a disk remains independent of r, i.e.

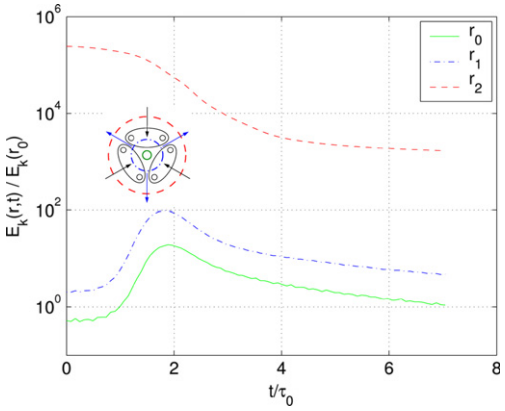

Figure 13. Kinetic energy $E_k(t)$ at different disk-like zones on the collision plane at $Re = 500$. The disk diameters are $(r_0, r_1, r_2)/D_0 = (0.05, 0.2, 1.0)$.

$$\frac{\mathrm{d}}{\mathrm{d}r}\left\langle E_k(r,\,t)\right\rangle\Big|_{r\leqslant r_0} = 0$$

In figure 13 we plot the kinetic energy on a disk of radius r centered on the collision point and normalized by $E_k(r_0)$. The kinetic energy in the safe zone, $E_k(r_0)$, starts to rise at $t/\tau_0 \sim 1$, the instant when the rings make contact, reaching a peak as a result of the flow reversal produced by the onset of secondary structures moving radially outwards. Here τ_0 is the time at the inflection point of the curve $E_k(r_2)$. Clearly, as $r \to \infty$, the kinetic energy $E_k(r)$ becomes the total kinetic energy of figure 11(b) as expected.

In order to properly work as an hydrodynamic trap, the collision should be performed periodically, i.e. we must repeat the ring emission with time intervals such that if a particle enters the collision zone it will remain trapped for longer periods, as it cannot leave the safe zone unless we stop the ring emission. In a gravitational field, the performance of a trap of this kind capturing small particles should depend on its orientation with respect to the gravity vector $\vec{g}$ (Uchiyama and Yagami 2008). This is an effect to consider when testing the trap capabilities, as diverging streamlines along $\pm z$ directions may be produced by the two secondary vortex rings originating after a collision.

3.6. Ring collision in water

In order to capture more details of the ring interaction, we built a water set-up to track and record the collision with a classic optical method, the shadowgraph (Rasenat *et al* 1989). This compact set-up (figure 14) consisted of a closed-volume chamber made from two concentric cylinders. At the inner cylinder's wall three brass tubes of internal diameter $D_0 = 0.42$ cm and 1 cm long were mounted flush, forming an angle of 120° between them. A homogeneous pressure pulse applied in the chamber between both cylinders pushes a ring from each brass tube into the inner region filled with distilled water at standard conditions. All rings have good fluid dynamic similarity (size and self-induced velocity) at low Reynolds numbers ($Re = 250$) and the experiment is relatively simple compared with the air set-up.

To get good quality and enhanced shadowgraphs, a fluid sugar solution at 1% (w/w) of refraction index n_2 fills the volume chamber which receives a pressure pulse producing three vortex rings completely filled with this fluid of index n_2. These rings propagate and will

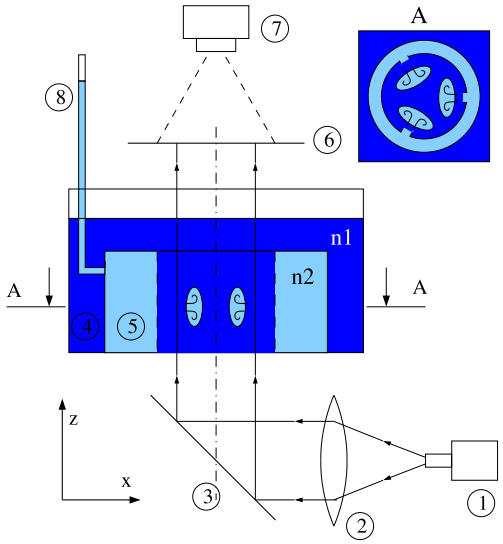

Figure 14. Shadowgraph set-up. A white light source (1) is expanded and collimated by a lens (2), then reflected in a mirror (3). The light strikes a Plexiglas bottom wall and propagates through the inner volume of refraction index n_1. The fluid of refraction index $n_2 = 1.35$ fills the volume between both concentric cylinders which is pushed by the pressure pulse forming three vortex rings which will collide. The ultimate image of the collision is projected into a screen (6) and then recorded with a ccd camera (7).

collide immersed in a fluid of different refraction index n_1 (distilled water), producing high contrast in the final shadowgraph. The gradient of the refraction index, $\mathrm{d}n/\mathrm{d}z$, is accumulated in the direction of parallel light rays, thus the high image contrast means a high gradient of the index (Smits and Lim 2010). Within the accuracy of this particular optical method it is possible to determine clear spatial limits of the scalar substance of index n_2 bounded by the fluid of index n_1.

Figures 15(a) and (b) are shadowgraphs at two time instants where we clearly distinguish the vortex ring bubble and vortex core. The vortex ring bubble is defined by the thin black line. In figures 15(c) and (d) the vortex rings have made contact, initiating the coupling of the vortex tubes of opposite circulation which produce the observed vortex pairing. Those arched arm-like vortex structures move away from the collision point resulting in the expanded structure of figures 15(e) and (f). The reconnection scheme is, including the vortex pairing, almost the same found in the observations with the air experiment on figures 6(c) and (d). The wake tracks observed in figures 15(e) and (f) are the result of the accumulated influence in the light propagation across the whole vortex structure contributing to the shadowgraph, which makes it difficult to have an overall view of the collision. This is the reason why the shadowgraph may not be the best technique to capture the complete tridimensional vortex structure. Instead, simple ink injection performed in the internal chamber of the water experiment provides a clear view of the final tridimensional vortex structure formed during collision. In figures 16(a) and (b) we see the ring-dominated stages before collision, followed by figures 16(c) and (d) which display clearly the 3D structure with their expanding arms which finally give life to the top and bottom vortex rings indicated with arrows in the figures 16(e) and (f).

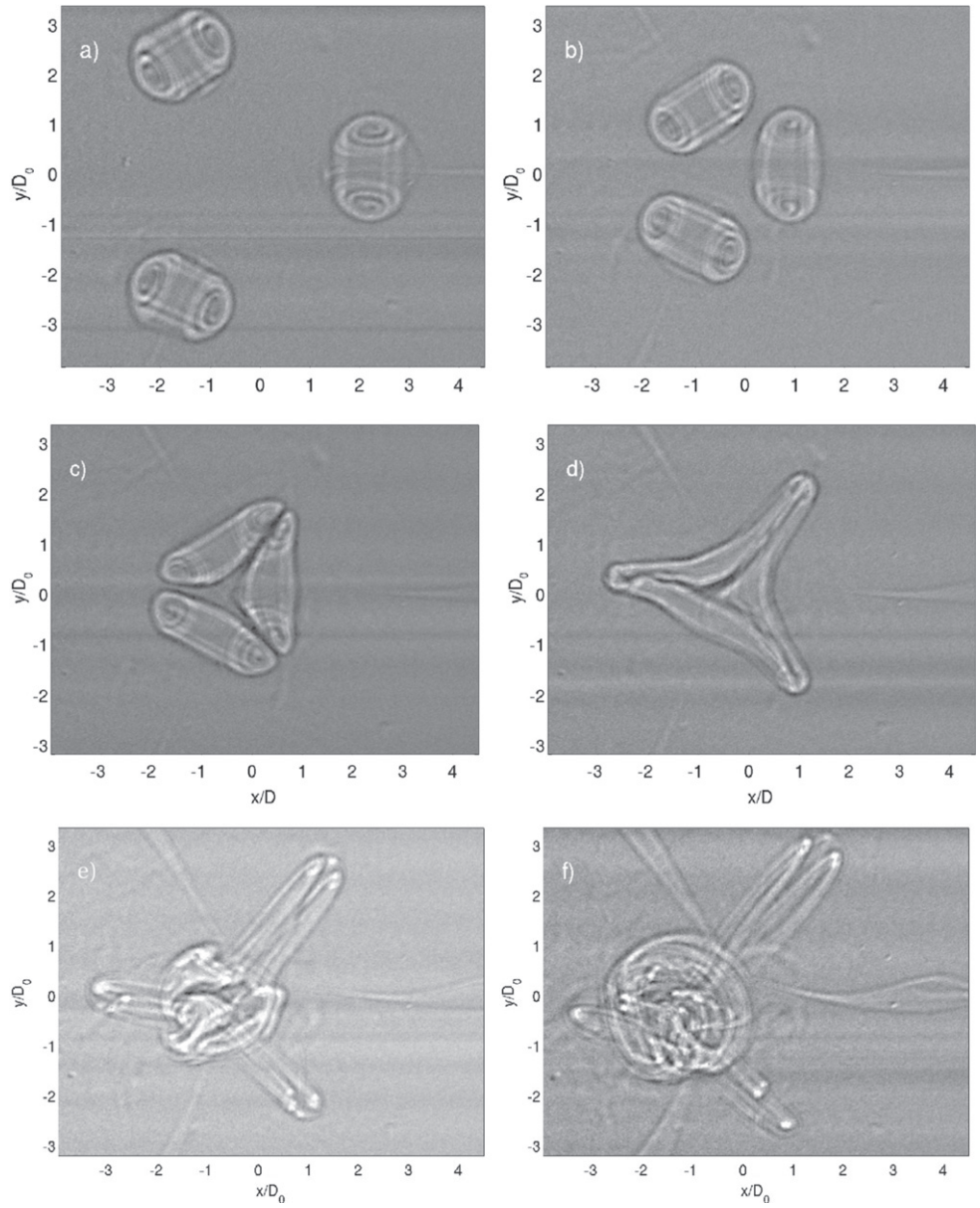

Figure 15. Shadowgraph of the collision. Vortex rings were filled with a fluid of refraction index $n_2 = 1.35$, obtained with a 1% (w/w) sugar solution, a passive scalar being transported into a clean distilled water region (buoyancy effects are not seen). (a) $t = 0.42$ s, (b) $t = 0.58$ s, (c) $t = 0.68$ s, (d) $t = 0.92$ s, (e) $t = 1.28$ s, (f) $t = 2.18$ s. $Re = 250$, $D_0 = 0.42$ cm.

4. Conclusions

We have investigated experimentally, for the first time, the interaction and simultaneous collision of three stable and laminar vortex rings where the adjacent angle between their pre-

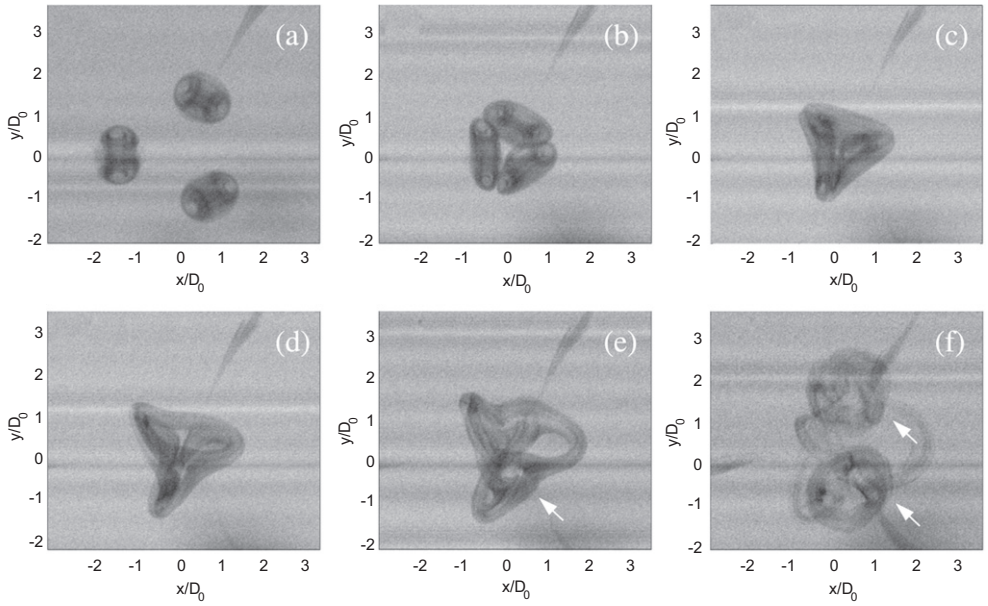

Figure 16. 3D view of the collision using ink visualization. The three vortex rings were created in distilled water and tagged with ink which is transported as a passive scalar into the collision region. Arrows indicate vortex rings formed after collision. (a) $t = 0.566$ s, (b) $t = 0.733$ s, (c) $t = 0.8$ s, (d) $t = 0.9$ s, (e) $t = 1.033$ s, (f) $t = 1.8$ s. $Re = 250$, $D = 0.42$ cm.

collision paths was 120°. Experiments in air and water under carefully controlled conditions allowed us to measure the instantaneous spatial structure of the colliding rings at several Reynolds numbers using both hot-wire anemometry and optical methods. At low Reynolds numbers, $Re < 400$, ring trajectories display small differences between each realization producing irregular collisions. At Reynolds numbers in the range $500 < Re < 950$, ring collisions involve a very regular fluid motion, assuring a good collision repeatability (thousands of realizations). After collision, there is reconnection of both top and bottom portions of the vorticity tubes of each vortex ring, a phenomenon that was observed both in air and water experiments.

Hot-wire measurements and flow visualizations allowed us to identify two main collision stages. A ring-dominated stage where rings experience a slowdown in the increase of their size, followed by a dipolar-dominated stage where we observed that opposite circulation vortex tubes are coupled and create local vortex pairs which make the whole structure expand in radial directions, rapidly dissipating kinetic energy. At higher Reynolds numbers, $Re > 1000$, we observed a rapid transition to turbulence from the very instant of the collision, presumably accelerated by the growth of vortex ring instabilities developed during pre-collision ring motion. A center collision zone of finite size was found to have the lowest kinetic energy during the entire process, presumably because the symmetries of the problem make the collision center a stagnation point. The preserved collision symmetries leading to the weak kinematic activity in the center zone makes this vortex structure a candidate for further studies to evaluate its performance and behavior as a periodic hydrodynamic trap to capture small and lightweight particles.

Moreover, it seems that simultaneous collisions involving more than 3 vortex rings may favor merging of side-by-side vortex tubes and should be investigated in a future work. In such configurations the contact angle between adjacent ring paths would be smaller than in this work, and it would be possible to avoid the onset of expanding arm-like vortex structures observed in the present work.

Acknowledgments

We want to thank Pintita for her endless support. Fondecyt grant no. 1085020 is gratefully acknowledged.

References

Afanasyev Y D and Korabel V N 2004 *Phys. Fluids* **16** 3850–8
Arévalo G 2010 Experimental study on the interaction between vortex rings in a 3D topology *PhD Thesis* Universidad de Chile, Santiago, Chile
Arévalo G, Hernández R H, Nicot C and Plaza F 2007 *Phys. Fluids* **19** 083603
Arévalo G, Hernández R H, Nicot C and Plaza F 2010 *Phys. Fluids* **22** 053604
Bentley B J and Leal L G 1986 *Appl. Phys. Lett.* **167** 219–40
Cantwell B J 1986 *J. Fluid Mech.* **173** 159–89
Chatelain P, Kivotides D and Leonard A 2003 *Phys. Rev. Lett.* **90** 054501
Fohl T and Turner J S 1975 *Phys. Fluids* **18** 433–6
Heijst G J F V and Flor J B 1989 *Nature* **340** 212–5
Hernández R H, Cibert B and Bechét C 2006 *Europhys. Lett.* **75** 743–9
Hwang W and Eaton J K 2004 *Exp. Fluids* **36** 444–54
Kambe T, Minota T and Takaota M 1993 *Phys. Rev.* E **48** 1866–81
Kida S, Takaoka M and Hussain F 1991 *J. Fluid Mech.* **230** 583–646
Krieg M and Mohseni K 2013 *J. Fluid Mech.* **719** 488–526
Leweke T and Williamson C H K 1998 *J. Fluid Mech.* **360** 85–119
Lim T and Nickels T 1992 *Nature* **357** 225–7
Oshima Y 1977 *J. Phys. Soc. Jpn.* **44** 328–31
Rasenat S, Hartung G, Winkler B L and Rehberg I 1989 *Exp. Fluids* **7** 412–20
Shariff K and Leonard A 1992 *Ann. Rev. Fluid Mech.* **24** 235–79
Smits A J and Lim T T 2010 Flow visualization, techniques and examples (London: Imperial College Press)
Stewart K C and Vlachos P P 2012 *Exp. Fluids* **53** 1033–44
Sullivan J P, Widnall S E and Ezekiel S 1973 *AIAA J.* **11** 1384–9
Tanyeri M, Johnson-Chavarria E M and Schroeder C M 2010 *Appl. Phys. Lett.* **96** 224101
Taylor G I 1934 *Proc. R. Soc. Lond.* A **146** 501–23
Uchiyama T and Yagami H 2008 *Powder Technol.* **188** 73–80
Voropayev S I and Afanasyev Y D 1992 *J. Fluid Mech.* **236** 665–89
Voropayev S I, Afanasyev Y D, Korabel V N and Flippov I A 2003 *Phys. Fluids* **15** 3429–33
Walker J and Smith C 1987 *J. Fluid Mech.* **181** 99–140
Widnall S E and Sullivan J P 1973 *Proc. R. Soc. Lond.* A **332** 335–53
Widnall S E and Tsai C Y 1977 *Phil. Trans. R. Soc. Lond.* **287** 273–305